

**AFRL-PR-WP-TP-2006-266**

**A COMPUTATIONAL ASSESSMENT  
OF INDEPENDENT STAGE  
CONTROL OF A CASCADE  
INJECTOR (POSTPRINT)**



**H.L. Meichenheimer, E.J. Gutmark, C.D. Carter, D.R. Eklund,  
and M.R. Gruber**

**OCTOBER 2006**

**Approved for public release; distribution is unlimited.**

**STINFO COPY**

**The U.S. Government is joint author of the work and has the right to use, modify,  
reproduce, release, perform, display, or disclose the work.**

**PROPULSION DIRECTORATE  
AIR FORCE MATERIEL COMMAND  
AIR FORCE RESEARCH LABORATORY  
WRIGHT-PATTERSON AIR FORCE BASE, OH 45433-7251**

| <b>REPORT DOCUMENTATION PAGE</b>  |   |   |   | <i>Form Approved</i><br>OMB No. 0704-0188  |   |   |  |                                  |
|---|---|---|---|--|---|---|--|----------------------------------|
| The public reporting burden for this collection of information is estimated to average 1 hour per response, including the time for reviewing instructions, searching existing data sources, gathering and maintaining the data needed, and completing and reviewing the collection of information. Send comments regarding this burden estimate or any other aspect of this collection of information, including suggestions for reducing this burden, to Department of Defense, Washington Headquarters Services, Directorate for Information Operations and Reports (0704-0188), 1215 Jefferson Davis Highway, Suite 1204, Arlington, VA 22202-4302. Respondents should be aware that notwithstanding any other provision of law, no person shall be subject to any penalty for failing to comply with a collection of information if it does not display a currently valid OMB control number. <b>PLEASE DO NOT RETURN YOUR FORM TO THE ABOVE ADDRESS.</b>   |   |   |   |  |   |   |  |                                  |
| <b>1. REPORT DATE (DD-MM-YY)</b><br>October 2006  |   | <b>2. REPORT TYPE</b><br>Conference Paper Postprint |   | <b>3. DATES COVERED (From - To)</b><br>N/A   |   |   |  |                                  |
| <b>4. TITLE AND SUBTITLE</b><br>A COMPUTATIONAL ASSESSMENT OF INDEPENDENT STAGE CONTROL OF A CASCADE INJECTOR (POSTPRINT)   |   |   |   | <b>5a. CONTRACT NUMBER</b><br>In-house   |   |   |  |                                  |
|   |   |   |   | <b>5b. GRANT NUMBER</b>  |   |   |  |                                  |
|   |   |   |   | <b>5c. PROGRAM ELEMENT NUMBER</b><br>61102F  |   |   |  |                                  |
| <b>6. AUTHOR(S)</b><br>H.L. Meichenheimer and E.J. Gutmark (University of Cincinnati)<br>C.D. Carter, D.R. Eklund, and M.R. Gruber, (AFRL/PRAS)   |   |   |   | <b>5d. PROJECT NUMBER</b><br>2308  |   |   |  |                                  |
|   |   |   |   | <b>5e. TASK NUMBER</b><br>AI   |   |   |  |                                  |
|   |   |   |   | <b>5f. WORK UNIT NUMBER</b><br>00  |   |   |  |                                  |
| <b>7. PERFORMING ORGANIZATION NAME(S) AND ADDRESS(ES)</b><br><table border="0" style="width: 100%;"> <tr> <td style="width: 50%; vertical-align: top;">           University of Cincinnati<br/>           Department of Aerospace Engineering<br/>           Cincinnati, OH         </td> <td style="width: 50%; vertical-align: top;">           Propulsion Sciences Branch (AFRL/PRAS)<br/>           Aerospace Propulsion Division<br/>           Propulsion Directorate<br/>           Air Force Research Laboratory, Air Force Materiel Command<br/>           Wright-Patterson AFB, OH 45433-7251         </td> </tr> </table>  |   |   |   | University of Cincinnati<br>Department of Aerospace Engineering<br>Cincinnati, OH  | Propulsion Sciences Branch (AFRL/PRAS)<br>Aerospace Propulsion Division<br>Propulsion Directorate<br>Air Force Research Laboratory, Air Force Materiel Command<br>Wright-Patterson AFB, OH 45433-7251 | <b>8. PERFORMING ORGANIZATION REPORT NUMBER</b><br>AFRL-PR-WP-TP-2006-266 |  |                                  |
| University of Cincinnati<br>Department of Aerospace Engineering<br>Cincinnati, OH   | Propulsion Sciences Branch (AFRL/PRAS)<br>Aerospace Propulsion Division<br>Propulsion Directorate<br>Air Force Research Laboratory, Air Force Materiel Command<br>Wright-Patterson AFB, OH 45433-7251 |   |   |  |   |   |  |                                  |
| <b>9. SPONSORING/MONITORING AGENCY NAME(S) AND ADDRESS(ES)</b><br>Propulsion Directorate<br>Air Force Research Laboratory<br>Air Force Materiel Command<br>Wright-Patterson AFB, OH 45433-7251  |   |   |   | <b>10. SPONSORING/MONITORING AGENCY ACRONYM(S)</b><br>AFRL-PR-WP                   |   |   |  |                                  |
|   |   |   |   | <b>11. SPONSORING/MONITORING AGENCY REPORT NUMBER(S)</b><br>AFRL-PR-WP-TP-2006-266 |   |   |  |                                  |
| <b>12. DISTRIBUTION/AVAILABILITY STATEMENT</b><br>Approved for public release; distribution is unlimited.   |   |   |   |  |   |   |  |                                  |
| <b>13. SUPPLEMENTARY NOTES</b><br>Conference paper published in the Proceedings of the 2006 42nd AIAA/ASME/SAE/ASEE Joint Propulsion Conference and Exhibit, published by AIAA.<br><br>The U.S. Government is joint author of the work and has the right to use, modify, reproduce, release, perform, display, or disclose the work. PAO case number: AFRL/WS 06-1459; Date cleared: 08 June 2006. Paper contains color.  |   |   |   |  |   |   |  |                                  |
| <b>14. ABSTRACT</b><br>A computational assessment of independent stage control of a cascade injector was performed. This investigation used computational fluid dynamics to gain understanding of the mechanics governing the penetration characteristics of the cascade injector. Comparison to experimental data, the effects of the first injection stage, and a turbulence model study are presented. The computational solutions predicted penetration height with good accuracy compared to the experimental data, based on planar laser-induced fluorescence of the NO molecule, but were not as successful predicting injectant plume width. Penetration in the near-field was found to correspond with the position of the shock wave generated by the injectant. The Menter turbulence model produced higher values of eddy viscosity in the vicinity of the plume and more spreading, which agreed better with the experimental data. The computational data was also used to generate a synthetic laser-induced fluorescence signal, which was used to improve the penetration boundary prediction. |   |   |   |  |   |   |  |                                  |
| <b>15. SUBJECT TERMS</b>  |   |   |   |  |   |   |  |                                  |
| <b>16. SECURITY CLASSIFICATION OF:</b><br><table border="1" style="width: 100%; border-collapse: collapse;"> <tr> <td style="width: 33%; padding: 2px;"><b>a. REPORT</b><br/>Unclassified</td> <td style="width: 33%; padding: 2px;"><b>b. ABSTRACT</b><br/>Unclassified</td> <td style="width: 33%; padding: 2px;"><b>c. THIS PAGE</b><br/>Unclassified</td> </tr> </table>  |   |   | <b>a. REPORT</b><br>Unclassified  | <b>b. ABSTRACT</b><br>Unclassified   | <b>c. THIS PAGE</b><br>Unclassified   | <b>17. LIMITATION OF ABSTRACT:</b><br>SAR                                 |  | <b>18. NUMBER OF PAGES</b><br>20 |
| <b>a. REPORT</b><br>Unclassified  | <b>b. ABSTRACT</b><br>Unclassified  | <b>c. THIS PAGE</b><br>Unclassified                 |   |  |   |   |  |                                  |
|   |   |   | <b>19a. NAME OF RESPONSIBLE PERSON (Monitor)</b><br>Campbell D. Carter<br><b>19b. TELEPHONE NUMBER (Include Area Code)</b><br>N/A |  |   |   |  |                                  |

# A Computational Assessment of Independent Stage Control of a Cascade Injector

H.L. Meichenheimer\* and E.J. Gutmark†

Department of Aerospace Engineering  
University of Cincinnati  
Cincinnati, Ohio

C.D. Carter,‡ D.R. Eklund,§ and M.R. Gruber‡

Aerospace Propulsion Division, Air Force Research Laboratory  
Wright Patterson AFB, Ohio

**A computational assessment of independent stage control of a cascade injector was performed. This investigation used computational fluid dynamics to gain understanding of the mechanics governing the penetration characteristics of the cascade injector. Comparison to experimental data, the effects of the first injection stage, and a turbulence model study are presented. The computational solutions predicted penetration height with good accuracy compared to the experimental data, based on planar laser-induced fluorescence of the NO molecule, but were not as successful predicting injectant plume width. Penetration in the near-field was found to correspond with the position of the shock wave generated by the injectant. The Menter turbulence model produced higher values of eddy viscosity in the vicinity of the plume and more spreading, which agreed better with the experimental data. The computational data was also used to generate a synthetic laser-induced fluorescence signal, which was used to improve the penetration boundary prediction.**

## I. Introduction

ONE of the main factors governing combustion efficiency in a supersonic flowpath is the design of the fuel injection system. High flow velocities in the combustor create short residence times, thereby requiring mixing and combustion processes to occur rapidly. Fuel injector designs for supersonic combustion ramjet (scramjet) engines balance penetration into the high-speed flow, with dispersion and mixing. To achieve the approximate balance, a variety of fuel injection techniques have been studied. These techniques can be divided into two classes. In-stream injectors, like struts and physical ramps, physically intrude into the flowpath and must be designed to maintain structural stability within the extreme environment of the combustor.<sup>1</sup> Wall jets do not physically intrude into the flowpath, but create a complex local flow around the injector<sup>1</sup> which remains an active area of research interest today.

It has long been known that material injected into a supersonic cross-flow creates a strong shock pattern and produces a complex region of flow.<sup>2</sup> Staged injection was found to alter the shock structure and characteristics typically used to evaluate injection: penetration and mixing rate.<sup>3,4</sup> In the early 1990's, researchers at the University of Virginia used laser-induced iodine fluorescence to nonintrusively investigate staged injection into a supersonic cross-flow.<sup>5</sup> Data collected using this diagnostic provided data that could be used for comparison to CFD solutions.<sup>6</sup> In 1997, Eroglu and Breidenthal used flow visualization techniques, including laser-induced fluorescence (LIF), to study a fully exponential transverse jet. In this injection concept, an exponential increase in injection width and velocity with downstream position were used to control penetration and mixing characteristics.<sup>7</sup>

---

\* Graduate Student, Member AIAA.

† Professor and Ohio Eminent Scholar, Associate Fellow AIAA

‡ Senior Aerospace Engineer, Associate Fellow AIAA.

§ Senior Aerospace Engineer, Senior Member AIAA.

The cascade injector block used in this study was developed by Aerojet General Corporation for use in scramjet engines. It is a staged injection technique designed to produce high levels of penetration across a high momentum air stream. The concept purportedly enables fueling large engines from flowpath walls, minimizing the need for more intrusive fueling schemes. The injector block, shown in Figure 1, is a lateral array of three cascade injectors. Each injector is composed of fourteen injection ports that are grouped into four axial stages. Each stage is supplied by a separate fuel manifold, as shown in Figure 2. Experimental and computational studies were completed by researchers at Wright Patterson AFB in 2000.<sup>8,9</sup>

Computations of the injectant flow performed by Cox-Stouffer et al.<sup>8</sup> used the VULCAN (Viscous Upwind aLgorithm for Complex Flow ANalysis) Navier-Stokes code.<sup>10</sup> By assuming symmetry along the tunnel centerline, a half-tunnel computational domain was used. Freestream Mach number, total pressure, and total temperature were specified to be 3, 265.5 kPa, and 303 K, respectively. Overexpanded, pressure-matched, and underexpanded fuel injection cases were studied. The pressure-matched and underexpanded cases were found to provide an excess level of penetration, suggesting incorrect scaling of the injector with respect to duct height. A 1.1 million node grid proved to provide sufficient resolution. The computational domain extended from the facility plenum, through the Mach 3 nozzle, and through the 2.0 inch high by 6.0 inch wide constant-area test section of the experimental facility. The numerical results showed good agreement with corresponding experimental data collected by Mathur et al.<sup>9</sup>

Based on recommendations from these previous investigations, Meicenheimer et al. explored independent stage control of the Aerojet cascade injector using the Air Force Research Laboratory's Research Cell 19 facility in 2005.<sup>11</sup> Of the three injectors shown in Figure 1, only the center cascade injector was used in this study. Each of the four stages was independently supplied with fuel and could be turned on and off using a ball valve (Figure 2). By examining combinations of active stages while maintaining a constant injection pressure condition (i.e., constant mass flow rate through a given active stage from case to case), the effects on penetration and mixing were observed. The injector was tested at two overexpanded injection conditions (144 psia, and 250 psia) in a Mach-3 crossflow. Shadowgraph and schlieren imaging, Mie scattering, and Nitrogen Oxide Planar Laser-Induced Fluorescence (NO-PLIF) were used to determine various features of the injectant plume and its interaction with the supersonic crossflow. A shadowgraph image of the baseline case, where all four cascade stages are active with an injection pressure of 144 psia, is shown in Figure 3. In Figure 4, an instantaneous side-view NO-PLIF image illustrates the typical injection plume structure for the baseline case. The bottom edge of the image corresponds to the bottom wall of the wind tunnel test section. The study concluded that penetration distance could be controlled by adjusting the number of active stages in the cascade. The first and second stages were determined to have the most significant effect on penetration distance per unit mass flow rate. The authors recommended further experimental and numerical study to increase understanding of the penetration and mixing characteristics.

This study continues the investigation of independent stage control of the Aerojet cascade injector. Computational fluid dynamics is used to explore the mechanics governing the penetration and mixing characteristics of the cascade injector.

## II. Numerical Approach

### Computer Code and Modeling

The computational results were obtained using the VULCAN Navier-Stokes code.<sup>10</sup> This code solves the Reynolds-averaged conservation equations (in 2-D, axisymmetric, or 3-D form) appropriate for calorically or thermally perfect gases with a cell-centered finite volume scheme. The equation set can be integrated in a fully elliptic or space-marched manner. The inviscid fluxes can be evaluated with central differences, Roe's flux difference method, or a low-diffusion flux vector split scheme. A variety of one-equation and two-equation turbulence model options can be chosen to describe the turbulent velocity field and assumed PDF options exist for modeling turbulence-chemistry interactions. Chemical reactions are accounted for with finite rate kinetics models based on the law of mass action. Although VULCAN is a structured solver, it can solve grids that are not continuous across block boundaries (non-C(0) continuous connectivity). The code also contains a number of other features, including full multi-grid capabilities and block level parallelization using MPI. Further description of this code and its capabilities can be found in the literature.<sup>10,12</sup>

The calculations in this study were performed using the low dissipation flux-split scheme of Edwards, derived for a mixture of thermally perfect gases. The Van Leer flux limiter was applied and the MUSCL parameter ( $\kappa$ ) was set to  $\frac{1}{3}$  to minimize truncation error. Solutions were advanced in time with a CFL number that started at 0.1 and was increased to a constant value of 4.0 as the initial transient behavior subsided.

For the majority of the cases in this study, turbulence was modeled using the 1998 Wilcox  $k-\omega$  model without the Pope correction term.<sup>13</sup> Previous studies have employed this model to examine injection into a supersonic cross-flow.<sup>14,15</sup> However, in order to complete a turbulence model study, two cases were run using other models. In the first case, turbulence was modeled using the Menter model.<sup>16</sup> This two-equation model applies the Wilcox  $k-\omega$  model<sup>6</sup> near the tunnel wall, then transitions to the Jones and Launder  $k-\epsilon$  model<sup>17</sup> in the outer edge of the boundary layer. In the second case, the explicit algebraic Reynolds-stress model of Gatski and Speziale<sup>18</sup> was applied with the Wilcox  $k-\omega$  model.<sup>13</sup> For all cases, the turbulent Prandtl and Schmidt numbers were set to constant values of 0.89 and 0.5, respectively.

### Computational Domain and Grids

The computational domain extended from the entrance plane of the isolator through the 2.0 inch high by 6.0 inch wide experimental facility test section. The cascade injector was located in the bottom wall of the test section, which had a 2.5 degree divergence. A single cascade injector was modeled. The injectant flow field from the discharge plane to the top wall of the test section was modeled on a half-tunnel computational domain with 1.4 million grid points. This grid was created with Gridgen, a commercial meshing toolkit used to create three-dimensional grids for complex geometries.<sup>19</sup> A two-dimensional image of the injector region of the grid is shown in Figure 5. Note that in this figure and all other side-view images, the grid coordinates have been transformed such that  $y = 0$  corresponds to the floor of the test section and the divergence is shown at the top of the domain.

### Boundary Conditions

The flow profile at the exit of the  $M = 3.0$  facility nozzle was provided as the inflow boundary condition of the isolator. This profile was obtained from the results of a simulation of heated air flow through the  $M = 3.0$  facility nozzle. Three chemical species were considered in all simulations. The freestream was defined as a mixture of 77% Nitrogen and 23% Oxygen. The injectant was air, defined within VULCAN to be a mixture of 75% Nitrogen, 23% Oxygen, and trace amounts of Carbon Dioxide and Argon. Injectant properties at the exit planes of the injection ports were defined using experimental measurements. For all cases where direct comparison was possible, the computational injectant mass flow rates had a less than 1% difference from the experimental data. Top, bottom, and side walls of the test section were considered to be adiabatic. A symmetry condition was applied along the tunnel centerline for the entire domain. The variables at the exit of the domain were extrapolated.

### Test Conditions and Solution Technique

This study consisted of the investigation of 10 cases which were subdivided into three areas of interest. The first was a comparison of three cases corresponding to the experimental conditions listed in Table 1. Case 1 served as a baseline case while Cases 2 and 5 demonstrated the impact of stages 4 and 1, respectively. The second study explored the impact of the first stage in the cascade, which was determined experimentally to have the greatest effect on penetration distance per unit mass flow rate.<sup>11</sup> In these simulations, the injection pressure of the first stage was incrementally increased from the baseline value of 144 psia to 250 psia while the other three stages were maintained at the baseline value. Finally, a turbulence model study was conducted. This study compared the Wilcox  $k-\omega$  model to the Menter model and the Gatski and Speziale explicit algebraic Reynolds-stress model.

Convergence for all cases was determined by examining the residual as well as the mass-averaged one-dimensional flow properties. The residual was observed to drop approximately 5.5 orders of magnitude before leveling off to a constant value. At this point, the mass-averaged one-dimensional flow properties showed little variation with respect to the number of iterations and the case was considered to be converged. Most cases reached convergence after 6,000 iterations.

### III. Results and Discussion

#### Comparison to Experimental Data

In the experimental data, the raw end-view images were corrected for perspective distortion and normalized using a reference image to remove the effects of laser sheet intensity distribution, collection efficiency, and camera fixed pattern noise. A background image was subtracted from each plume image, and then the images were ensemble-averaged. Each average image was normalized by its maximum NO LIF signal. Penetration distance and the maximum plume width were determined using a Matlab code. The penetration distance was defined to be the maximum vertical position having at least 10% of the maximum signal. Maximum injection plume width was the largest difference between the first and last occurrence of 10% of the maximum signal at a given transverse position in the jet plume.

The raw side-view images were processed in manner similar to the end-view images. Because the camera was positioned in an orientation normal to the tunnel test section, a perspective distortion correction was not necessary. The reference images required to correct for the laser sheet intensity distribution, collection efficiency, and camera fixed pattern noise were not acquired during experimental testing. Although it was not possible to completely account for these variations, the effects were mitigated by using a running average of the local maximum NO signal to normalize the images. The upper plume penetration boundary was defined using 10% of this average local maximum. Because scattering off of the bottom wall of the test section may have affected the NO signal strength, 25% of the average local maximum signal was used to define the lower plume penetration boundary. These boundaries were identified for each case using a Matlab code.

The penetration boundaries for the CFD data were defined using the injectant mass fraction instead of the NO signal data. These boundaries were determined using Matlab codes that were consistent with the experimental data analysis. The upper boundary of the side-view penetration distance was determined by 10% of the running average of the local maximum NO signal. The NO signal strength used to define the lower penetration boundary in the side-view was 25% of the local maximum signal; a higher value was used to mitigate the effect of scattering off of the floor of the tunnel test section. In the end-view, the dispersion boundary was defined as 10% of the local maximum NO signal.

Figures 6a and b present a comparison of the side-view and end-view plume penetration boundaries of the experimental and computational data for Case 1, respectively. In the side-view, the penetration boundaries correspond in the region around the injector, but become increasingly divergent with downstream position. In Case 1, the computational data begins to over-predict the upper and lower penetration boundaries at approximately  $x = 0.68$  inches and  $x = 1.16$  inches, respectively. At the end of the experimental data domain, this over-prediction is 0.10 inches in magnitude for the upper boundary and 0.11 inches in magnitude at the lower boundary. In the end-view, the CFD data increasingly under-predicts the plume width with increasing downstream position. For Case 1 at  $x = 3.5$  inches, the magnitude of this under-prediction is approximately 0.19 inches. The trends of over-predicting penetration height in the side-view and under-predicting plume width in the end-view are present for all cases and both pressure conditions, as indicated in Table 2.

In both the experimental and computational data, the upper penetration boundary in the near field of the injector corresponds with the location of the shock wave caused by the injectant. This observation is illustrated using the CFD data in Figures 7 and 8. In these figures, the penetration boundary defined by 10% of the maximum injectant mass fraction is shown on a contour plot of the static pressure. In the region around the injector, the penetration boundary is aligned with the increase in static pressure that denotes the location of the shock wave.

Figures 7 and 8 also show the increase in penetration that is obtained by increasing the injection pressure. These figures clearly show a greater increase for Case 2 than for Case 5. This occurrence, which is consistent with previous experimental data analysis<sup>4</sup>, seems to indicate the importance of the first stage. Stage 4, which has the largest area and therefore supplies the most injectant mass flow, is not active in Case 2, so a small increase in mass flow rate results in a significant increase in penetration distance.

### First Stage Pressure Increase

Figures 9a and b show a side-view and end-view comparison of cases with an incremental increase in the injection pressure of the first stage. These figures show an average incremental increase in penetration of approximately 0.025 inches per 53 psia of injection pressure. Because increasing the injection pressure of Stage 1 does not have a significant impact on penetration, this stage cannot be solely responsible for the penetration increase observed in Figure 7. Rather, this increase appears to be due to an increase in shock angle caused by the increase in mass flow. In Figures 10a, b, and c, there is no observable increase in shock angle because increasing the injection pressure of Stage 1 causes a minimal increase in overall mass flow rate. The shock angle increases 3 degrees between Figures 8a and b. Between Figures 7a and b, there is a 9-degree increase in shock angle. Both of these more substantial increases are caused by a significant increase in mass flow.

This conclusion is further supported by Figure 11, which displays streamlines overlaid on a plot of static pressure contours for Case 1. Streamlines, which are tangential to the local velocity vectors, indicate the location and amount of turning that occurs in the flow. As shown in the figure, these streamlines coalesce to form a definite boundary which governs the static pressure field. Both the core flow and the flow from the injector turn as they intersect each other. This turning creates the strong pressure waves that form shock waves in the flow. The location of the inflection point of the streamline defines the penetration boundary. At a higher pressure, the flow coming from the injector is able to travel a farther distance before it intersects the free stream flow and forms the shock, which results in increased penetration.

### Turbulence Model Study

A comparison of the Wilcox  $k-\omega$  model, Menter model, and Gatski and Speziale explicit algebraic Reynolds-stress model to the experimental data for Case 1 is shown in Figure 12. The side-view penetration distance at the end of the experimental domain and the  $x = 3.5$  inch end-view plume width at the location of the maximum experimental plume width are presented in Table 3. Although the Gatski and Speziale algebraic Reynolds-stress models over-predicts the penetration in the side-view by a greater distance than the Wilcox  $k-\omega$  model, both schemes under-predict the plume width in the end-view by approximately the same amount. The Menter model is observed to under-predict both penetration and plume width. However, the Menter model under-predicts the plume width by a lesser amount than either of the other models.

The differences in the flowfields are best illustrated using the side-view and end-view contours of the eddy viscosity ratio which are displayed in Figures 13, 14, and 15. The eddy viscosity ratio, defined as the eddy viscosity divided by the molecular viscosity<sup>12</sup>, can be considered a measure of the turbulent transport of momentum to the molecular, or laminar, transport of momentum. The lower penetration distance and larger plume width predicted by the Menter model are the result of the larger turbulent transport. As the turbulent viscosity increases, the mass diffusion due to turbulence, which is a function of the turbulent viscosity and the injectant species gradient, also increases. In Figure 15b, the Menter model exhibits higher eddy viscosity ratio values indicative of larger turbulent viscosity within the plume penetration boundary. Also, the turbulent transport of momentum reduces the strength of the vorticity of the injection plume, as illustrated in Figure 16.

### Synthetic LIF Signal

The NO LIF signal depends on the local values of static temperature and pressure. Because this signal is not equivalent to the injectant mass fraction, the CFD solution was used to generate a synthetic LIF signal, which is shown in Figure 17a. Figures 17b-d show the static pressure, static temperature and injectant mass fraction fields from the CFD solution that were used to create the synthetic signal. The calculated temperature and pressure were used to derive ground-state Boltzmann fraction, net electronic quenching rate<sup>20</sup>, and the laser-transition overlap integral relative to an arbitrary reference condition. These factors were then used to calculate the relative fluorescence signal from the computed injectant number density. The NO concentration in the injectant was about 200 parts per million, PPM; this concentration was set by mixing air with gas from the NO bottle, which contained 10,000 PPM (1% by volume) of NO in N<sub>2</sub>. This concentration, 200 PPM, was sufficient for a strong fluorescence signal, but the injectant consisted of mostly air. Among the species present in the injectant, only O<sub>2</sub> was a significant quencher of the excited NO. Other chemical species with large quenching cross sections (e.g., NO) were considered but existed only in small concentrations. Although the electronic quenching cross section for NO-O<sub>2</sub> collisions shows little variation at and above room temperature<sup>20</sup>, no values have been reported at the low-

temperature condition encountered in this work. It should also be noted that the laser-transition overlap integral did not include the effect of the collisional pressure shift.

The penetration boundary defined by the synthetic LIF signal is displayed in Figures 17a-e. This boundary was determined using a Matlab code consistent with those used to determine the penetration boundaries for the experimental and CFD data. The upper and lower penetration boundaries, respectively, represent 10% and 25% of the local maximum synthetic LIF signal for each axial position.

Figure 17 illustrates the relationship between the synthetic LIF signal (Figure 17a), the CFD solution (Figures 17b-d), and the experimental data (Figure 17e). The shape and intensity of the injection plume seen in Figure 17e is clearly reflected in Figure 17a. Because the CFD solution does not contain the effects of scattering that are seen in the experimental data, the synthetic LIF signal structure is more distinct. The synthetic LIF signal shows details of the injection from the individual ports that compose the cascade. These features are not well-defined in the static pressure or mass fraction contours from the CFD solution, but they are observed in the experimental data, and are pronounced in the static temperature field. This observation highlights the strong dependence of the synthetic signal on the static temperature field.

The side-view penetration boundaries defined by the synthetic LIF signal, experimental data, and CFD solution are compared in Figure 18. The CFD solution models Case 1 with an injection pressure of 144 psia using the Wilcox  $k-\omega$  turbulence model. The synthetic LIF signal reduces the amount of over-prediction for the upper penetration boundary with respect to the experimental data and improves the accuracy of the Wilcox  $k-\omega$  model prediction. Despite this improvement, sources of uncertainty combined with the relatively small difference between the penetration boundaries defined by the synthetic LIF signal and the injectant mass fraction, indicate that the injectant mass fraction remains a valid parameter for comparison to the NO fluorescence.

#### IV. Conclusions and Recommendations

A better understanding of the mechanisms governing the penetration and mixing characteristics of the cascade injector was gained through the use of computational fluid dynamics. All solutions were found to be consistent with previously analyzed experimental data and similar trends were observed. The computational data showed overall excellent agreement in terms of penetration distance, but was significantly less accurate in predicting plume width. As observed in the experimental data, the first stage produced the greatest effect on penetration distance per unit mass flow rate. However, an incremental increase in the injection pressure of the first stage did not produce a significant increase in penetration. By examining the static pressure and streamlines in the CFD solution, changes in penetration were attributed to the amount of turning that occurred in the flow field. Increasing the injection pressure of Stage 1 produced a minimal increase in the overall mass flow rate and did not alter the location of the shock wave, so there was no corresponding increase in penetration distance. Further study on the effect of stage 1 by simulating injection through stages 2 and 3 only is recommended by the authors.

A turbulence model study showed that the Wilcox  $k-\omega$  model and the Gatski and Speziale explicit algebraic Reynolds stress model over-predicted the amount of penetration and under-predicted the plume width. The Menter model was observed to under-predict both the penetration height and the plume width. It produced larger eddy viscosity values in the region surrounding the injection plume, resulting in a lower penetration distance and larger plume width. In addition to the eddy viscosity ratio, the turbulent transport of mass and energy are governed by the turbulent Schmidt and Prandtl numbers, respectively. Variation of these numbers will alter the injection plume characteristics and may offer increased understanding of the effects of transport phenomena. Because only the effects of the turbulence model on the baseline case were examined in this study, the authors also recommend that a turbulence model study be conducted on Case 2 and Case 5. Large eddy simulation of all cases would provide additional insight into the plume structure and penetration characteristics.

The CFD data was used to generate a synthetic LIF signal, which was similar to the experimental NO-PLIF signal. Although the synthetic signal offered better agreement with the experimental data, this improvement was not great enough to invalidate the comparisons made using only the injectant mass fraction. Of course, some uncertainty exists in the electronic quenching rate due to the low static temperatures; ideally, future measurements



using NO LIF should be conducted at static temperatures at or above room temperature, to mitigate the uncertainty in the calculated electronic quenching cross section.

## V. Acknowledgements

This work was sponsored by Dr. J. Tishkoff with funding provided by the Air Force Office of Scientific Research. The Aerojet cascade injector was provided by Mr. M. Bulman of Aerojet General Corporation. Additional support was a grant of computer time on the SGI Origin 3900 provided by the ASC MSRC Department of Defense High Performance Computing Modernization Program at Wright Patterson AFB. Support from the staff of this center is recognized and appreciated. The authors also gratefully acknowledge Dr. R. Baurle and Dr. S. Cox-Stouffer for their technical contributions during the course of this study.

## VI. References

1. Kutschenreuter, P. Scramjet Propulsion. Curran, E.T. and Murthy, S.N.B., ed., "Chapter 8: Supersonic Flow Combustors." American Institute of Aeronautics and Astronautics, Inc. Reston, VA. 2000.
2. Zukoski, E.E., and Spaid, F.W. "Secondary Injection of Gases into a Supersonic Flow." *AIAA Journal*. Vol. 2, No. 10, 1964, pp.1689-1696.
3. Rogers, R.C. "Mixing of Hydrogen Injected from Multiple Injectors Normal to a Supersonic Airstream." NASA TND-6476, Sept. 1971.
4. Clement, P., and Rodriguez, C. "Shock Wave Structure and Penetration Height in Transverse Jets." *AIAA Student Journal*. Vol. 27, No. 2, 1989, pp. 7-16.
5. Hollo, S.D., McDaniel, J.C., and Hartfield, R.J., Jr. "Quantitative Investigation of Compressible Mixing: Staged Transverse Injection inot Mach 2 Flow." *AIAA Journal*. Vol. 32, No. 3, 1994, pp. 528-534.
6. Eklund, D.R., Northam, G.B., Dancey, C.L., and Wang, J.A. "Computational/Experimental Investigation of Staged Injection into a Mach 2 Flow." *AIAA Journal*. Vol. 32, No. 5, 1994, pp. 907-916.
7. Eroglu, A., and Breidenthal, R.E. "Exponentially Accelerating Jet in Crossflow." *AIAA Journal*. Vol. 36, No. 6, 1998, pp. 1002-1009.
8. Cox-Stouffer, S.K., Gruber, M.R., and Bulman, M.J. "A Streamlined, Pressure-Matched Fuel Injector for Scramjet Applications." AIAA Paper 2000-3707, 2000.
9. Mathur, T., Cox-Stouffer, S., Hsu, K.-Y., Crafton, J., Donbar, J., and Gruber, M. "Experimental Assessment of a Fuel Injector for Scramjet Applications." AIAA Paper 2000-3703, 2000.
10. White, J.A., and Morrison, J.H. "A Pseudo-Temporal Multi-Grid Relaxation Scheme for Solving the Parabolized Navier-Stokes Equations." AIAA Paper 99-3360, 1999.
11. Meichenheimer, H.L., Gutmark, E.J., Carter, C.D., Eklund, D.R., Gruber, M.R., and Hsu, K.-Y. "Independent Stage Control of a Cascade Injector." AIAA Paper 2005-3708, 2005.
12. Hypersonic Air-Breathing Propulsion Branch, NASA Langley Research Center. VULCAN homepage. <http://vulcan-cfd.larc.nasa.gov/>
13. Wilcox, D.C. Turbulence Modeling for CFD, Second Edition. DCW Industries, Inc., 2004.
14. Menter, F.R. "Zonal Two Equation k-w Models for Aerodynamic Flows." AIAA Paper 93-2906, 1993.
15. Baurle, R.A., Tam, C.-J., and Dasgupta, S. "Analysis of Unsteady Cavity Flows for Scramjet Applications." AIAA Paper 2000-3617, 2000.
16. Menter, F.R. "Improved Two-Equation k-w Turbulence Models for Aerodynamic Flows." NASA TM-103975, Oct. 1992.
17. Jones, W.P., and Launder, B.E. "The Calculation of Low-Reynolds Number Phenomena with a Two-Equation Model of Turbulence." *International Journal of Heat and Mass Transfer*, Vol. 16, 1973, pp.1119-1130.
18. Gatski, T.B., and Speziale, C.G. "On Algebraic Stress Models for Complex Turbulent Flows." *Journal of Fluid Mechanics*, Vol. 254, 1993, pp. 59-78.
19. Pointwise, Inc. Gridgen Overview. <http://www.pointwise.com/gridgen/>
20. Settersten, T.B., Patterson, B.D., and Gray, J.A.. "Temperature- and species-dependent quenching of NO  $A^2\Sigma^+$  ( $v' = 0$ ) probed by two-photon laser-induced fluorescence using a picosecond laser", in preparation.

Table 1: Experimental test matrix.

| Case # | Active Stages | Nominal Injection Pressure (psia) |
|--------|---------------|-----------------------------------|
| 1      | 1,2,3,4       | 144, 250                          |
| 2      | 1,2,3         | 144, 250                          |
| 5      | 2,3,4         | 144, 250                          |

Table 2: Experimental and computational data comparison (in inches).

| Low Injection Pressure  |   |       |   |       |  |       |                               |       |
|-------------------------|---|-------|---|-------|--|-------|-------------------------------|-------|
|                         | Side-view upper penetration<br>at x = 2.2 in. |       | Side-view lower penetration<br>at x = 2.2 in. |       | End-view Penetration<br>at x = 3.5 in. |       | Plume Width<br>at x = 3.5 in. |       |
| Case #                  | Experimental                                  | CFD   | Experimental                                  | CFD   | Experimental                           | CFD   | Experimental                  | CFD   |
| 1                       | 1.048   | 1.149 | 0.186   | 0.295 | 1.054                                  | 1.207 | 0.788                         | 0.425 |
| 2                       | 0.846   | 1.011 | 0.186   | 0.312 | 0.856                                  | 1.077 | 0.738                         | 0.380 |
| 5                       | 0.885   | 0.948 | 0.154   | 0.276 | 0.894                                  | 1.039 | 0.638                         | 0.380 |
| High Injection Pressure |   |       |   |       |  |       |                               |       |
|                         | Side-view upper penetration<br>at x = 2.2 in. |       | Side-view lower penetration<br>at x = 2.2 in. |       | End-view Penetration<br>at x = 3.5 in. |       | Plume Width<br>at x = 3.5 in. |       |
| Case #                  | Experimental                                  | CFD   | Experimental                                  | CFD   | Experimental                           | CFD   | Experimental                  | CFD   |
| 1                       | 1.356   | 1.449 | 0.247   | 0.292 | 1.451                                  | 1.604 | 0.650                         | 0.455 |
| 2                       | 1.096   | 1.321 | 0.269   | 0.386 | 1.108                                  | 1.398 | 0.713                         | 0.395 |
| 5                       | 1.029   | 1.056 | 0.279   | 0.352 | 1.07                                   | 1.154 | 0.638                         | 0.440 |

Table 3: Experimental data and turbulence model comparison (in inches).

|                                      | Side-view<br>upper penetration<br>at x = 2.2 in. | Side-view<br>lower penetration<br>at x = 2.2 in. | End-view<br>Penetration<br>at x = 3.5 in. | Plume Width<br>at x = 3.5 in. |
|--------------------------------------|--|--|---|-------------------------------|
| Experimental Data                    | 1.048  | 0.186  | 1.054                                     | 0.788                         |
| Wilcox k-w Model                     | 1.149  | 0.295  | 1.303                                     | 0.424                         |
| G.S. Algebraic Reynolds Stress Model | 1.235  | 0.285  | 1.207                                     | 0.439                         |
| Menter Model                         | 0.967  | 0.227  | 1.059                                     | 0.497                         |



Figure 1: Cascade injector block.

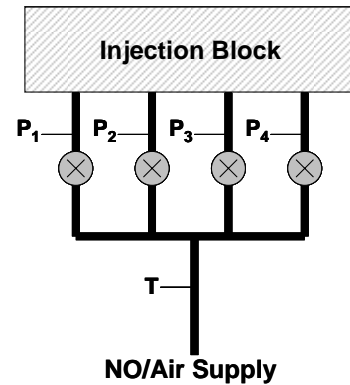


Figure 2: Diagram of fuel manifold with stagnation pressure and temperature measurement locations.

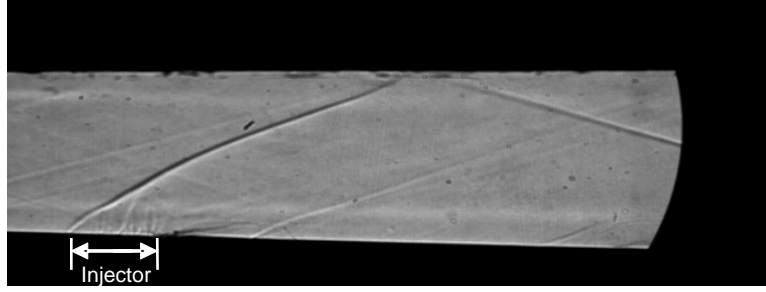


Figure 3: Shadowgraph image of baseline case,  $P_{inj} = 144$  psia.

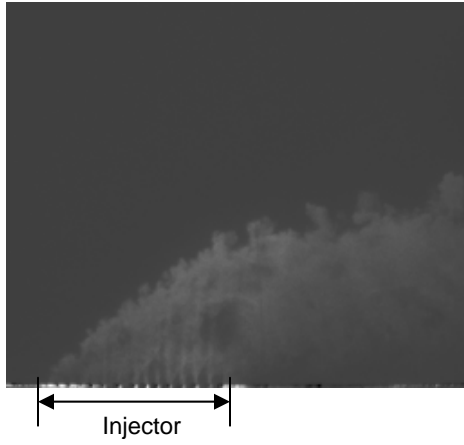


Figure 4: Instantaneous side-view NO-PLIF image of baseline case,  $P_{inj} = 144$  psia.

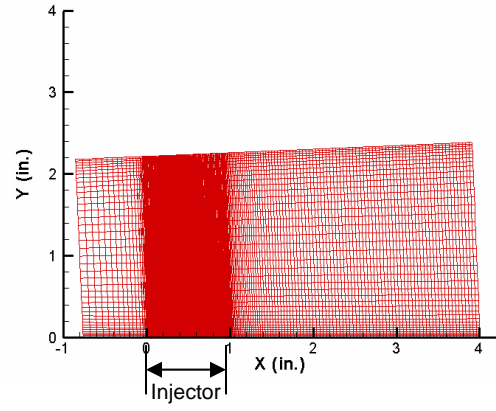
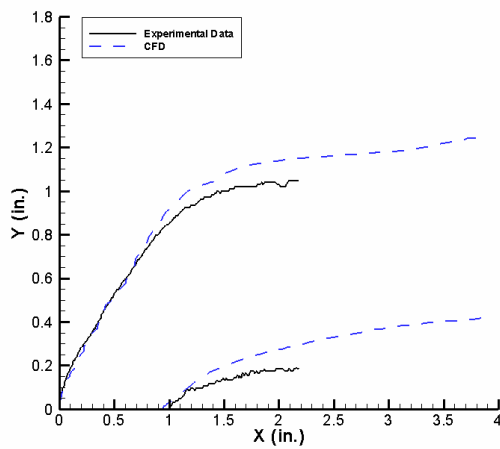
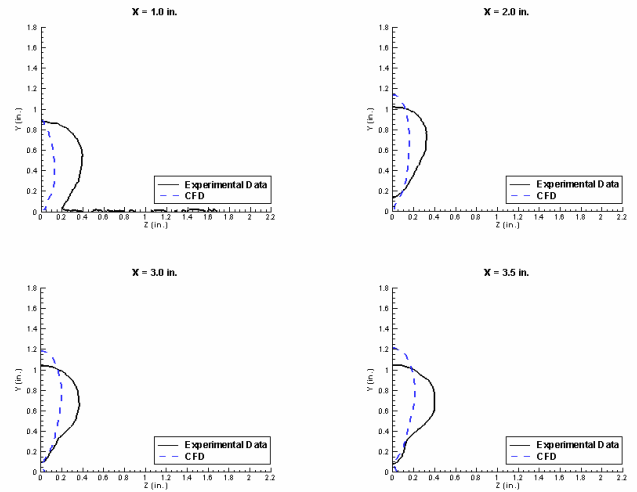


Figure 5: Grid system for region surrounding Aerojet cascade injector.

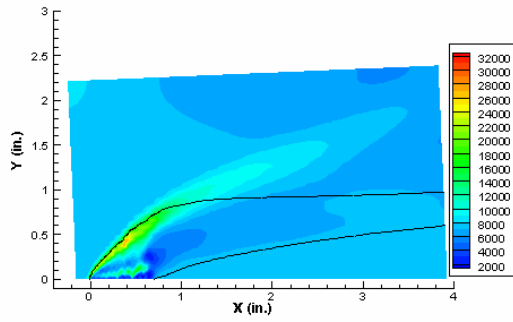


(a) Side-view.

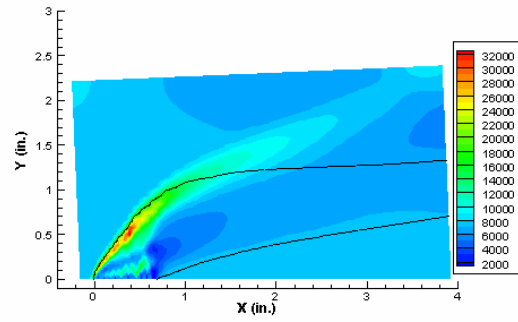


(b) End-view.

Figure 6: Comparison of CFD and experimental data for Case 1,  $P_{inj} = 144$  psia.

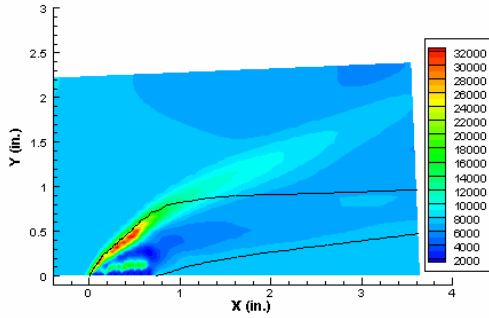


(a)  $P_{ini} = 144$  psia

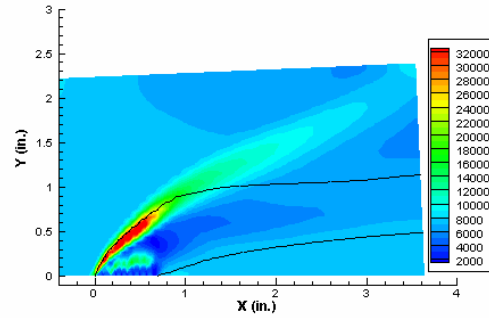


(b)  $P_{ini} = 250$  psia

Figure 7: Static pressure contours with penetration boundary for CFD Case 2.

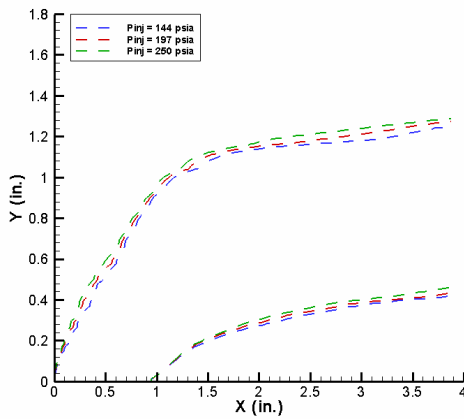


(a)  $P_{ini} = 144$  psia

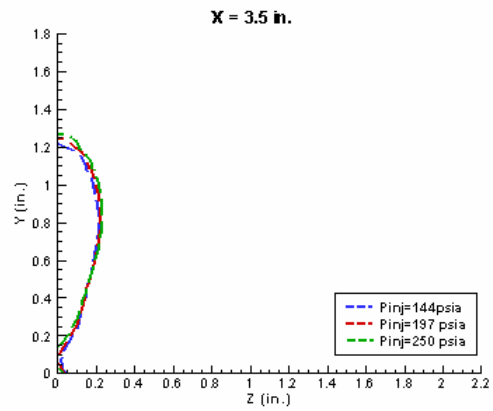


(b)  $P_{ini} = 250$  psia

Figure 8: Static pressure contours with penetration boundary for CFD Case 5.



(a) Side-view.



(b) End-view.

Figure 9: First stage pressure increase.

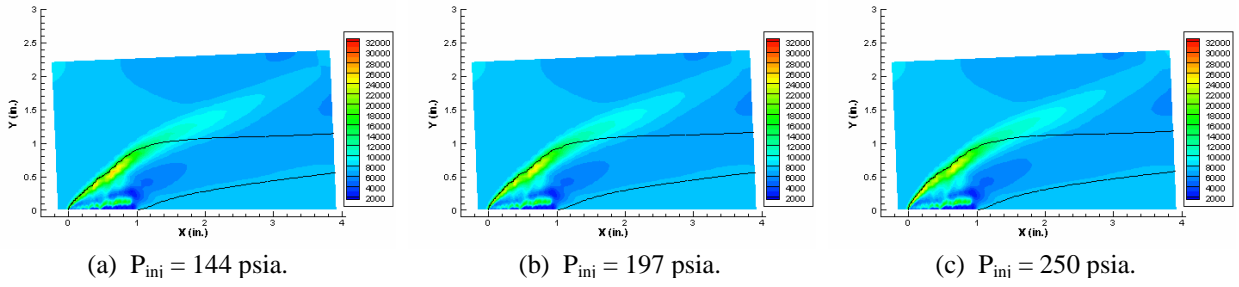


Figure 10: Static pressure contours with penetration boundary for first stage pressure increase.

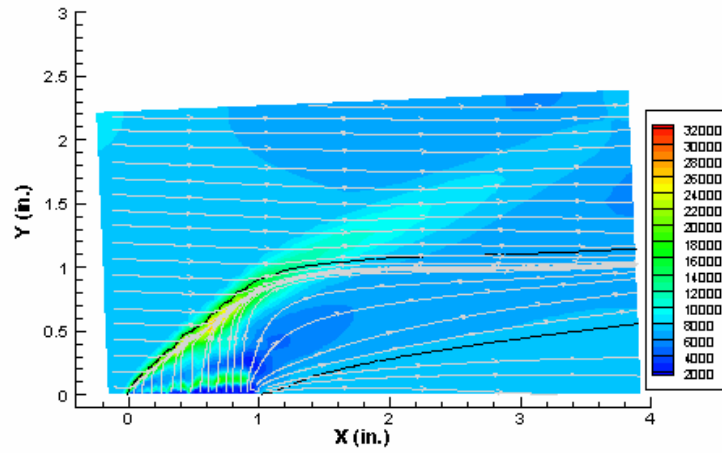


Figure 11: Static pressure contours with streamlines and penetration boundary for Case 1,  $P_{inj} = 144$  psia.

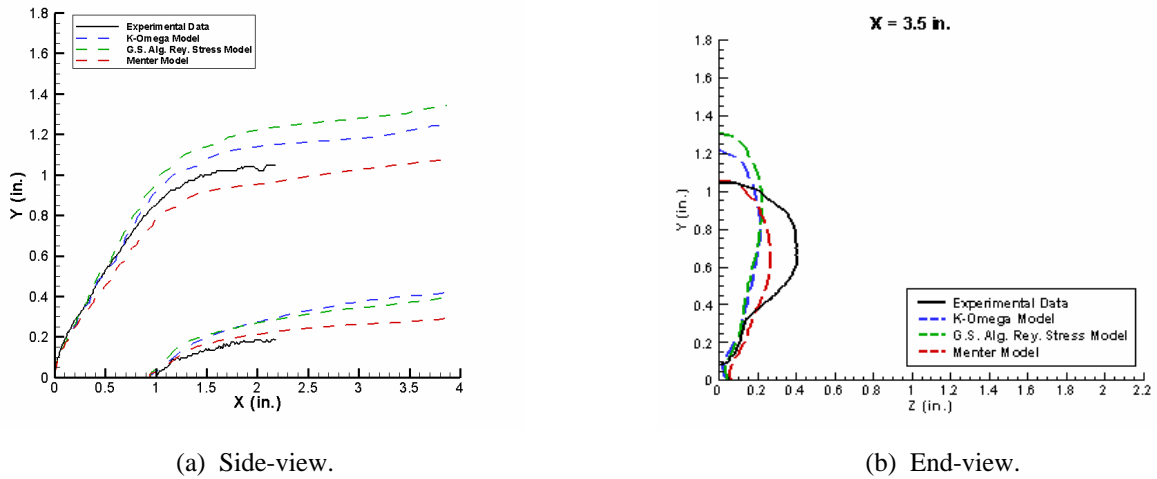


Figure 12: Turbulence model comparison.

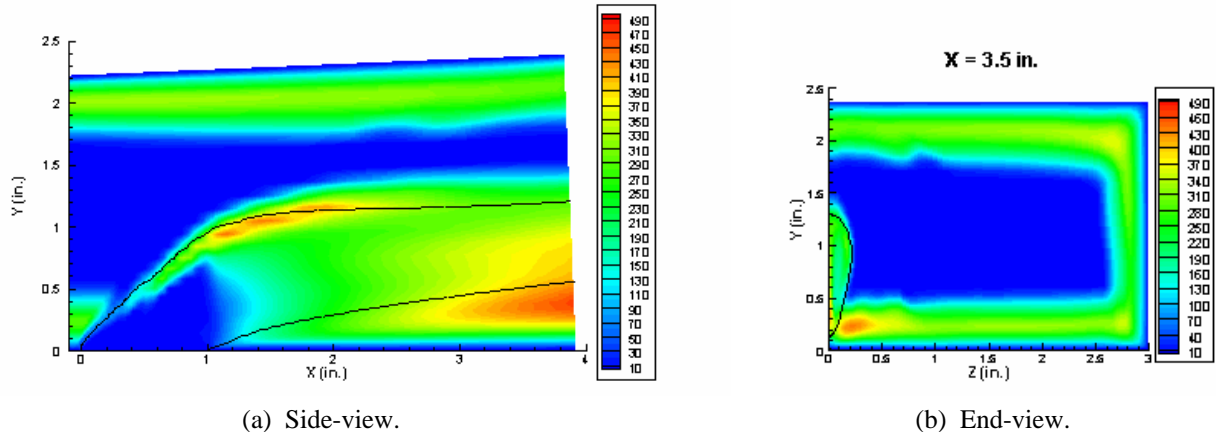


Figure 13: Gatski-Speziale algebraic Reynolds stress model eddy viscosity ratio.

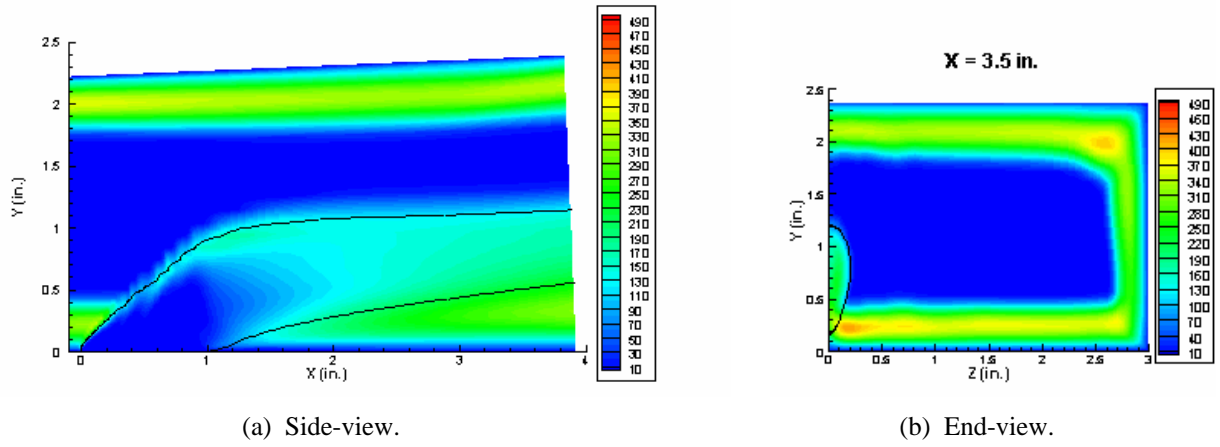


Figure 14: Wilcox k- $\omega$  model eddy viscosity ratio.

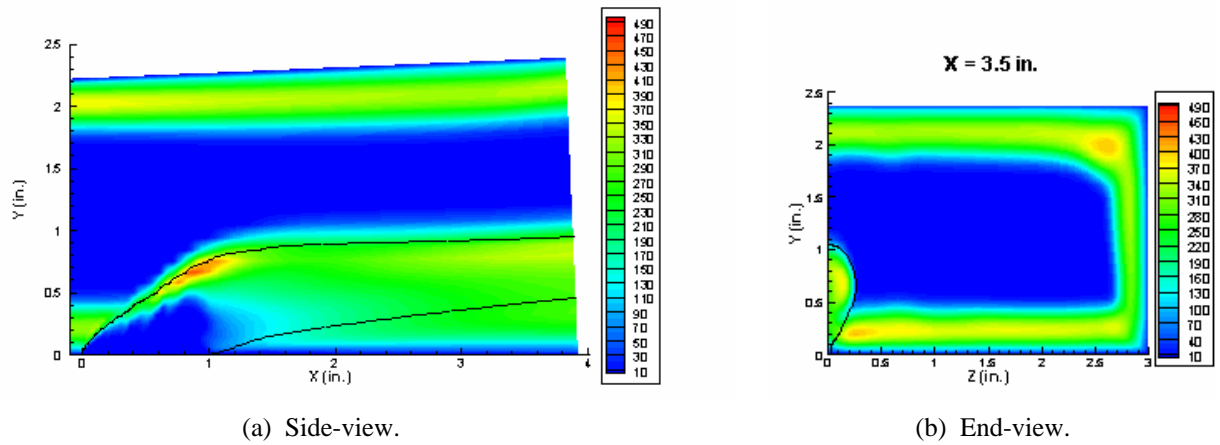


Figure 15: Menter model eddy viscosity ratio.

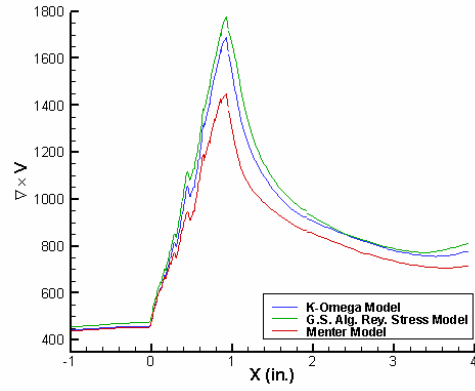
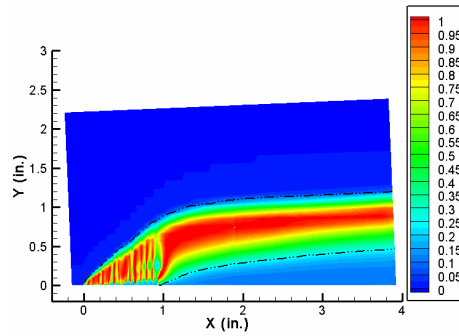
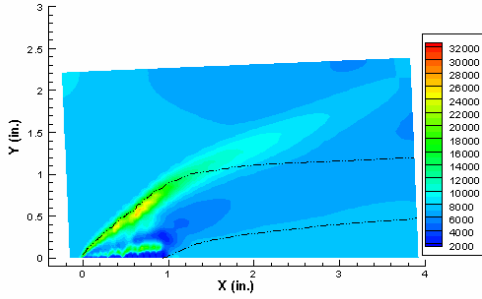


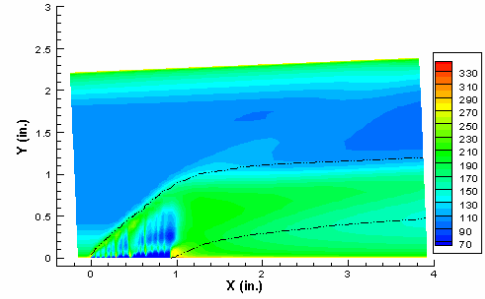
Figure 16: One-dimensional vorticity.



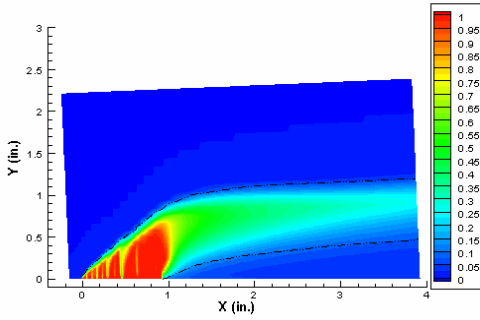
(a) Synthetic LIF signal.



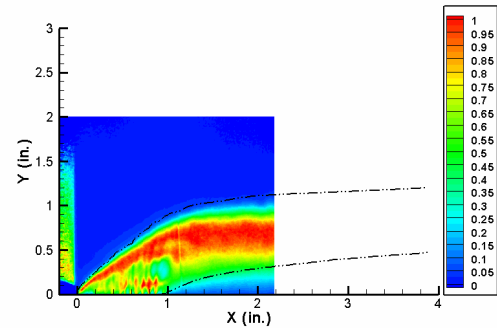
(b) Static Pressure Contours from CFD (Pa).



(c) Static Temperature contours from CFD (K).



(d) Mass Fraction contours from CFD.



(e) Experimental NO-PLIF signal.

Figure 17: Side-view contours with synthetic LIF signal penetration boundaries.

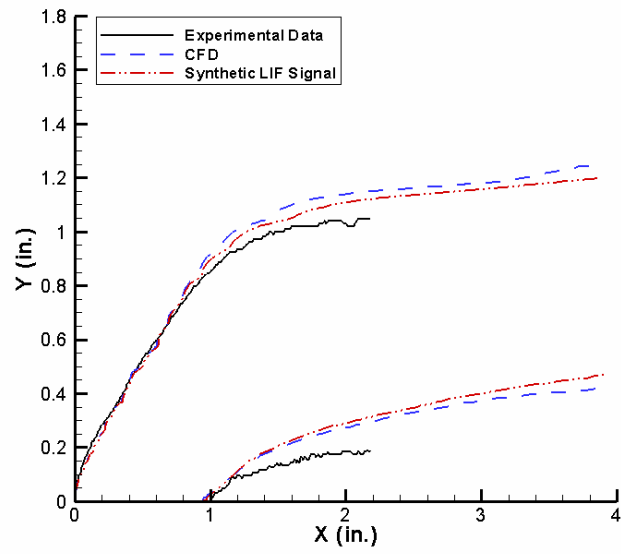


Figure 18: Side-view comparison of penetration boundaries.